Lab on a Chip

PAPER

View Article Online
View Journal | View Issue

Cite this: *Lab Chip*, 2026, **26**, 2734

Cap-Sweat: a capillary microfluidic platform for digitized sweat sampling and time-resolved biomarker analysis

Pezhman Jalali [ab] and Amir Sanati Nezhad *[ac]

Received 20th December 2025,
Accepted 23rd March 2026

DOI: 10.1039/d5lc01172h

rsc.li/loc

Wearable biofluid sampling systems are often limited by poor temporal resolution, evaporative loss, and dependence on glandular pressure for fluid propulsion. We present Cap-Sweat, a first-of-its-kind, ventless capillary microfluidic device that passively digitizes sweat into sequential, time-resolved compartments without requiring absorbent pads, hydrogels, or external actuation. Adapted from our Cap-Drop droplet platform for 3D cell culture, Cap-Sweat incorporates pre-programmed capillary circuits, multilayer laser-fabricated architecture, and hydrophilic–hydrophobic patterning to autonomously guide, delay, and arrest flow at discrete microchambers. A centralized, sealed venting mechanism prevents sample evaporation while maintaining bubble-free, pump-free operation. *In vivo* studies during exercise demonstrated continuous cortisol chrono-sampling with sub-minute resolution, capturing a transient early surge followed by fluctuating oscillations—dynamics that are undetectable using conventional continuous-flow or absorbent-based patches. This high-fidelity, temporally resolved biomarker profiling reveals previously obscured features of acute stress physiology and supports applications in neuroendocrine research, psychological health monitoring, and performance tracking. Cap-Sweat's compatibility with ELISA and future biosensor integration, combined with its scalable, low-cost design, positions it as a versatile platform for point-of-care diagnostics and personalized health analytics.

1 Introduction

Biomarker concentrations in biological fluids are inherently dynamic, influenced by circadian rhythms, physical activity, stress, and metabolic processes.[1] Capturing these temporal fluctuations—known as chrono-sampling—is crucial for accurate physiological assessments.[2] For instance, cortisol, a primary stress hormone, exhibits diurnal variations with peak levels in the early morning and gradual declines throughout the day.[3] Ignoring such temporal dynamics can lead to misinterpretations, potentially overlooking critical physiological or pathological events. Chrono-sampling has been instrumental in unveiling temporal biomarker patterns in various biofluids, including blood and saliva, elucidating hormonal cycles, metabolic fluxes, and responses to therapeutic interventions.[4] However, these methods often require invasive procedures or are limited by sample volume constraints. Sweat, being a non-invasive and readily accessible biofluid, presents an attractive alternative; however, its low secretion rates and susceptibility to evaporation pose challenges for accurate chrono-sampling.[5,6]

Advancements in materials science, mechanical design, and miniaturized electronics have facilitated the development of thin, soft, and skin-interfaced devices for chrono-sampling of biofluids, allowing more sophisticated analysis of physiological parameters.[1] Among biofluids, sweat is a promising medium for non-invasive health assessment due to its rich composition of electrolytes and metabolites.[7,8] Chrono-sampling of sweat is particularly valuable for tracking hydration status, electrolyte balance, and metabolic activity over time.[9–11] Advanced capabilities in non-invasive, *in situ* monitoring of sweating rate and sweat electrolyte losses could enable continuous personalized fluid-electrolyte intake recommendations, optimizing individual hydration strategies.[12,13] Wearable microfluidic devices provide a suitable approach for accurate sweat collection by isolating sweat from the skin and precisely capturing microliter-scale samples from well-defined skin regions.[9,13–21] The enclosed nature of these microfluidic systems reduces contamination risks and preserves biomarker integrity, which is crucial for applications in personalized medicine, athletic performance optimization, and military readiness.[22]

[a] *BioMEMS and Bioinspired Microfluidics Laboratory, Department of Biomedical Engineering, University of Calgary, Calgary, AB T2N 1N4, Canada. E-mail: amir.sanatinezhad@ucalgary.ca*
[b] *Biomedical Engineering Program, University of Calgary, Calgary, AB T2N 1N4, Canada*
[c] *Department of Mechanical and Manufacturing Engineering, University of Calgary, Calgary, AB T2N 1N4, Canada*

Traditional sweat sampling methods rely on absorbent pads, gauze, or filter paper, followed by centrifugation and benchtop analysis.[23] While effective in controlled laboratory settings, these approaches are prone to sample evaporation and contamination during transport from the patient's skin to the laboratory.[13,24] Additionally, material from the pad may introduce contaminants into the sweat sample, while the fiber matrix inside the pad can trap target biomarkers, potentially decreasing the accuracy of the final analysis. The motivation to maintain capillary pressure within the system has kept this method relevant, especially with the integration of nanofibers and hydrogels,[25] and by replacing post-analysis with real-time (online) monitoring. The growing interest in online, non-invasive detection has paved the way for the development of various sweat patches with innovative designs, most of which utilize a single channel to direct sweat through a detection area. This approach is well suited for sweat rate monitoring and biomarker detection, provided that a reliable online detection method is available.[26] However, these platforms are not capable of preserving sample chronology, as sweat is collected either through a shared absorbent pad or into a common channel, where newly secreted sweat mixes with previously collected samples.[27] This mixing limits the ability to analyze temporal variations in target biomarkers such as cortisol and cytokines, for which highly sensitive and selective techniques like ELISA or mass spectrometry are required.

An alternative microfluidic approach uses a single inlet connected to a series of sequentially filling microchambers (CHs), each linked to a main flow channel (MF) and equipped with vents for air release.[28–31] These designs support *in situ* sample collection and analysis while maintaining sample separation, ensuring that newly secreted sweat does not mix with previously collected samples. While these vents are necessary for proper fluid flow, they also act as evaporation sites. The evaporation effect is particularly critical for analytes present at low concentrations, where even minor losses can compromise data integrity.[32] Materials like polydimethylsiloxane (PDMS) also permit evaporation through the channel walls, especially under physiological temperatures. However, PDMS remains widely used due to its biocompatibility and optical transparency. To address evaporation, one method involves placing hydrophobic burst valves at chamber inlets, which enable bubble-free and sequential filling without requiring a vent at each CH.[33] However, this approach demands precise surface modification of PDMS, increasing fabrication complexity. Another strategy integrates fibers into each chamber to replace trapped air with sweat *via* capillary action.[34] Yet, fibers can trap biomarkers, introduce contamination, and complicate downstream analysis due to prolonged liquid extraction steps.[35]

From a fluidic perspective, wearable sweat patches fabricated from hydrophobic materials like PDMS, polyethylene terephthalate (PET),[36] or 3D-printed resins[37] inherently generate positive capillary pressure prior to any surface treatment. In these systems, sweat enters the MF and CH only when glandular pressure exceeds the channel's capillary resistance or the pressure threshold of embedded hydrophobic burst valves inside the system. This often necessitates sweat accumulation at the inlet and limits the use of narrow channels due to the high hydraulic resistance they impose. Even when the inlet region is rendered hydrophilic through hydrophilic fillers[20] or surface modification,[38] fluid transport remains predominantly pressure-driven because the downstream MF retain hydrophobic characteristics. In such architectures, fillers and surface treatments mainly reduce dead volume and facilitate sweat transfer from the skin to the channel entrance, rather than enabling sustained capillary-driven flow throughout the microfluidic network. Consequently, a critical unmet need remains for a wearable microfluidic platform capable of pressure-independent, ventless, and evaporation-resistant chrono-sampling while preserving strict sample chronology for offline, gold-standard biomarker analysis.

To address key limitations in droplet-based microfluidics —including reliance on external pumping, evaporation control, inconsistent droplet formation, and fabrication complexity, we previously introduced Cap-Drop, a self-powered capillary microfluidic platform designed for passive droplet digitization and high-throughput 3D cell culture.[39] Cap-Drop integrates a multilayer structure composed of hydrophilic PET and patterned hydrophobic pressure-sensitive adhesive (PSA), incorporating capillary elements such as stop valves (SVs), delay channels, pressure reducers, and passive vents to enable precise flow control and droplet immobilization without external pumps. Using this design, Cap-Drop can reliably digitize a range of biofluids, including blood, saliva, and hydrogels, into isolated 40–500 nL droplets with minimal cross-contamination and evaporation. Its compatibility with transparent, biocompatible materials and laser-based fabrication makes it a versatile, low-cost platform for biological assays and microscale tissue modeling.

Building upon this platform, we present Cap-Sweat, a wearable microfluidic system adapted from Cap-Drop for continuous sweat sampling (Fig. 1). While Cap-Sweat retains the core capillary architecture and droplet immobilization principles of Cap-Drop, it introduces critical modifications over its capillary circuit (CC) to accommodate sweat flow, enhance skin compatibility, support flexible substrates, and improve evaporation resistance. The system comprises sequential CH interconnected through a programmable CC that enables autonomous fluid handling. To our knowledge, this is the first wearable microfluidic system that enables pressure-independent, ventless chrono-sampling with deterministic sequential compartmentalization under physiological conditions. Sequential filling is governed by an engineered hierarchy of capillary forces and hydraulic resistances that directs fluid progression from one CH to the next independent of sweat secretion rate. Rather than relying on glandular pressure, hydrophobic capillary burst valves, or active flow control, the intrinsically hydrophilic CH and MF

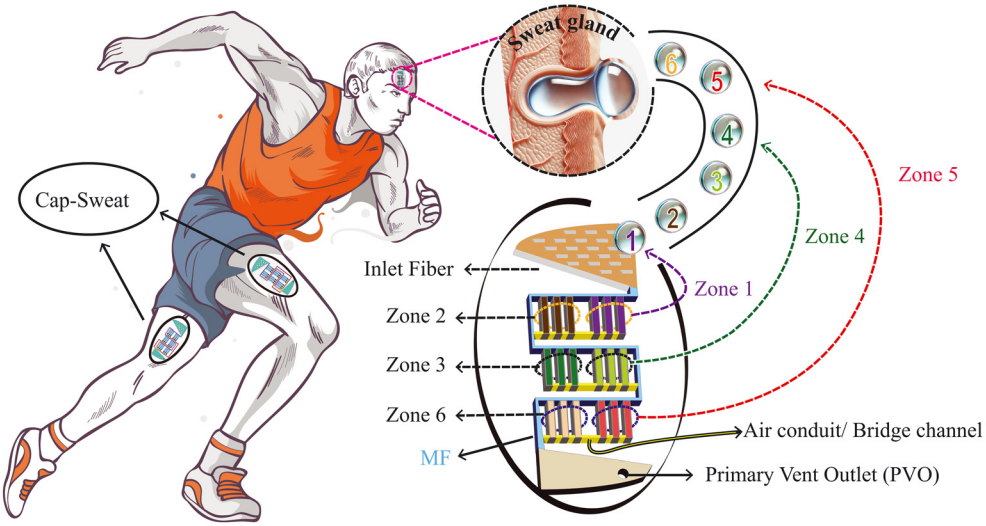

Fig. 1 Schematic illustration of the Cap-Sweat platform for wearable, chrono-resolved sweat sampling. The multilayer microfluidic system integrates a skin-interfacing inlet with a fiber, a main flow capillary channel (MF), a primary vent outlet (PVO), an air conduit, and six sequential collection zones, each containing three microchambers (CHs). Sweat secreted at the skin interface is passively transported through the programmable capillary network and sequentially compartmentalized in a deterministic filling order from zone 1 to zone 6, corresponding to progressively later secretions. This establishes a clear chronological mapping between collection zones and sampled sweat fractions. The architecture enables autonomous, non-invasive, time-resolved sampling of sweat directly from the skin during physical activity, operating entirely through capillary-driven flow.

surfaces enable spontaneous fluid uptake and capillary-driven transport, minimizing sweat accumulation at the inlet and ensuring robust operation across physiological conditions. This geometry-programmed capillary mechanism discretizes continuously generated sweat into sequential constant-volume samples, preserving temporal sample integrity and preventing mixing between successive fractions. By using non-breathable laminates and eliminating vent-related evaporation losses, Cap-Sweat preserves chrono-resolved sweat samples in discrete CH for offline biochemical analysis. During exercise studies, the system demonstrated its capability to quantify sweat rate dynamics and monitor temporal cortisol variations, highlighting its potential as a foundational platform for wearable bioanalysis, physiological monitoring, and biomarker discovery in health, fitness, and clinical applications.

2 Experimental section

2.1 Materials and reagents

Cellulose paper (CFP42-457) was obtained from SterliTech Inc. (USA) and used as the fiber. Hydrophilic PET film (3M 9984, USA) served as the top and bottom substrates for capillary flow. Hydrophobic PSA layers—ARcare® 8939, ARcare® 90106NB, and ARcare® 93049—were supplied by Adhesives Research Inc. (USA). These materials possess distinct optical and adhesive properties and were used as spacer layers (SPs) to define microfluidic features and control flow interfaces. The cortisol ELISA kit was purchased from Thermo Fisher Scientific (USA). All reagents used were of analytical grade unless stated otherwise.

2.2 Device fabrication

All layers of the Cap-Sweat wearable patch were designed using AutoCAD and fabricated through a sequential layer-by-layer process using a CO_2 laser cutter (Trotec Speedy 360 FLEXX, 80 W CO_2 and 30 W fiber laser). This approach enabled precise patterning and bonding of each SP layer before processing the next, allowing the laser to cut through already aligned, bonded layers without requiring manual realignment—akin to additive manufacturing. The multi-layer laminated structure included top and bottom sealing layers. To modulate the capillary driving force, one or both sealing layers were fabricated from hydrophilic PET. The intermediate SPs, made of hydrophobic PSA, were patterned to form the customized MF, CHs, SVs, and air conduits. Laser parameters were optimized to power 80%, speed 70%, frequency 5000 Hz, and two passes to ensure smooth channels without residue. A laser-cut wicking fiber (SterliTech CFP42-457) was embedded at the inlet to draw sweat from the skin into the MF.

The device incorporated six sequentially filling zones (each containing three consecutive CHs), together with a central MF, centralized venting network, SVs, and pressure-reduction steps to enable controlled, evaporation-free chrono-sampling. No external power sources, pumps, or burst valves were required.

2.3 Sweat collection and extraction protocol

All experiments were performed in accordance with the Guidelines of the University of Calgary Research Ethics Board, and experiments were approved by the ethics

committee at the University of Calgary (REB171310). Informed consent was obtained from all human participants in this study. Sweat samples were collected from healthy volunteers during a controlled treadmill exercise protocol. The Cap-Sweat patch was affixed to the upper back, thigh, or forehead using a biocompatible adhesive. Prior to attachment, the skin was cleaned with 70% ethanol pads, followed by rinsing and thorough drying. Each session lasted approximately 12–18 min, during which sweat was continuously collected. After the test, the patch was immediately placed on dry ice for 2 min to stabilize sweat droplets and minimize cross-diffusion between CHs. Following stabilization, the patch was sectioned into six individual zones, each corresponding to a distinct timepoint of sweat collection, as shown in Fig. 1. Sweat was extracted from each zone by centrifugation at 1000 rpm for 1 min. Extracted samples were stored at −20 °C prior to biochemical analysis.

2.4 Cortisol quantification

Cortisol levels in sweat were determined using a competitive enzyme-linked immunosorbent assay (ELISA) kit (Thermo Fisher, USA), following the manufacturer's protocol. Briefly, standards and sweat samples were pipetted into microplate wells pre-coated with cortisol antibodies. After incubation and washing steps, detection reagents were added, and color development was measured at 450 nm using a microplate reader. A standard calibration curve was generated (Fig. S6), and cortisol concentrations in each zone were quantified by interpolation. All assays were performed in triplicate. Time-resolved cortisol profiles were analyzed for physiological trends in response to exercise-induced stress.

3 Results and discussion

3.1 Design and working principle of Cap-Sweat

The Cap-Sweat platform is a multilayered, capillary-driven microfluidic system designed for temporally resolved collection of eccrine sweat under ambulatory conditions. Its architecture comprises a top sealing film, a micro-structured spacer region, and a basal substrate layer (Fig. 2). The final layer—referred to as the skin adhesive—is used to affix the device directly to the skin, eliminating the need for any external adhesive to maintain its position.

Two configurations were developed: Cap-Sweat Type-G, consisting of two SP layers, and Cap-Sweat Type-F, which incorporates three SP layers for enhanced functionality (Fig. 2a and b). In both formats, the hydrophobic SPs are constructed using medical-grade, double-sided PSA films, which simultaneously serve as bonding agents and structural elements. These PSA layers provide conformal adhesion across interfaces, maintaining fluidic integrity even under repetitive skin deformation encountered during motion or physical exertion. The modular nature of the Cap-Sweat assembly enables functional partitioning across layers and supports integration of diverse materials to tune capillary resistance, channel geometry, and surface energy—allowing

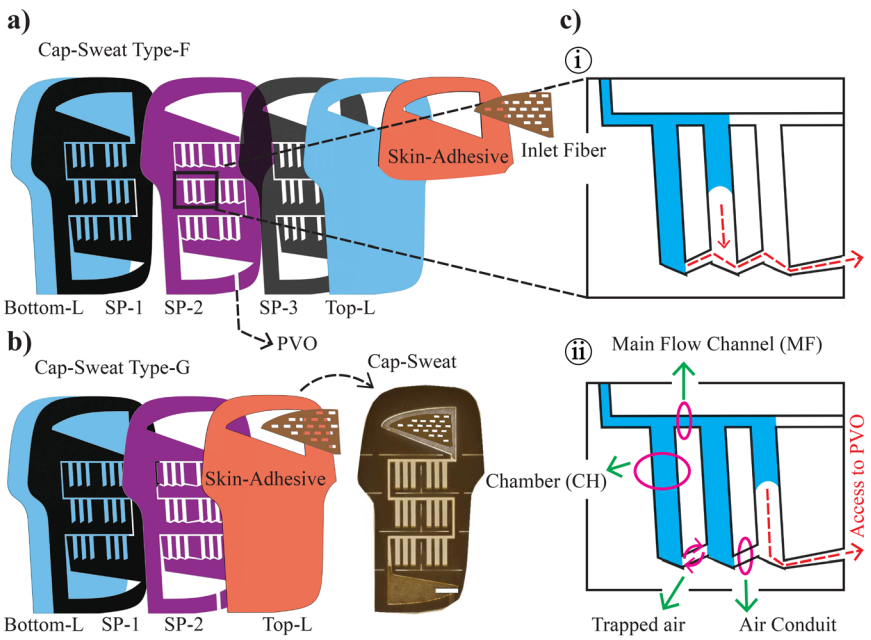

Fig. 2 Schematic overview of the Cap-Sweat architecture and internal capillary features for chrono-sampling of sweat. (a) Cap-Sweat Type-F with a series of capillary circuit (CC) features in a six-layer laminate structure, including three spacer (SP) layers sandwiched between hydrophilic top and bottom layers to promote uniform capillary wicking. (b) Cap-Sweat Type-G with a series of CCs adopted in a four-layer configuration in which the top layer is hydrophobic, facilitating dry reagent pre-loading, while the bottom layer remains hydrophilic to sustain fluid transport, scale bar: 5 mm. (c) (i) Close-up view of the passive, sequential loading mechanism *via* CCs, enabling orderly CH filling and air displacement. (ii) Enlarged schematic showing key microfluidic features including the MF, individual sweat collection CHs, integrated air conduits, and shared PVO access.

precise control of flow behavior without requiring capillary burst valves, active pumping, or mechanical actuation.

Capillary pressure in the Cap-Sweat system is controlled by tuning the surface wettability of the microchannel boundaries. In the Type-F configuration, both the upper and lower sealing layers are hydrophilic, which promotes uniform capillary action and spontaneous fluid propagation throughout the microfluidic network. In contrast, the Type-G configuration employs an asymmetric design consisting of a hydrophobic top surface and a hydrophilic base layer. Both configurations enable reliable capillary-driven transport across physiologically relevant sweat-rate conditions. However, Type-F requires additional SP layers, resulting in a thicker and mechanically stiffer multilayer structure. By contrast, Type-G achieves reliable fluid transport with fewer layers, leading to reduced device thickness, improved mechanical flexibility for conformal skin contact, and greater robustness to CO_2-laser fabrication variability, while maintaining sufficient capillary driving force independent of sweat-gland pressure (Table S1). Additionally, the hydrophobic surface in Type-G enables pre-functionalization of CHs through drop-casting of dry reagents prior to final lamination. This asymmetric wettability preserves robust capillary transport while enabling reagent preloading, thereby expanding the platform's capability for integrated sensing and biochemical analysis. Notably, all wearable experiments and chrono-sampling in this study were performed using the Type-F configuration, as its thicker collection chambers accommodate the larger sample volumes required for ELISA analysis.

As shown in Fig. 1 and 2, the Cap-Sweat device initiates fluidic operation *via* a single inlet positioned directly above an eccrine sweat gland. A laser-patterned porous fiber element is integrated at the inlet site to form a continuous capillary interface between the epidermis and the device, thereby establishing a low-resistance fluidic pathway for passive sweat uptake (Note S2). This fiber acts as both a wicking element and a flow stabilizer, ensuring consistent fluid transfer under low secretion rates and during dynamic skin movement. Upon entry, sweat is transported into the MF that traverses the length of the device and interfaces with a series of discrete CHs.

The standard Cap-Sweat configuration incorporates 18 CHs, providing a maximum operational volume of ~99–103 μL, while sampling begins once the first CH is filled at approximately ~18 μL (Note S7). The number and geometry of the CHs are readily adaptable to accommodate diverse application needs, including enhanced temporal granularity or increased sample volume for low-abundance biomarker analysis. In addition, the inlet geometry can be tuned to regulate sweat intake, enabling extended sampling durations. The detailed device dimensions are provided in Table S1.

To prevent uncontrolled lateral spreading despite the use of hydrophilic sealing layers, the device incorporates an engineered capillary pressure hierarchy and hydraulic resistance contrast that direct fluid into the collection CHs. The CHs are designed with a lower capillary entry barrier and reduced flow resistance relative to the adjacent MF, making CH filling energetically more favorable than lateral propagation along the MF (Note S1.3). This design ensures bubble-free flow, enabling deterministic fluid localization within the CHs, and preventing cross-contamination between sequential compartments. Accordingly, it preserves the chronology of sweat secretion for downstream biomarker analysis.

To facilitate continuous air displacement and mitigate pressure accumulation during fluid ingress, a centralized venting network is integrated into the chip architecture (Fig. 2c). Two CC architectures were evaluated: a parallel CC and a series CC. In this study, the series CC provided more robust performance under dynamic conditions, enabling consistent CH filling and reliable stop-valve operation in contact with sweat. In both designs, each CH is connected *via* air conduits to a shared primary vent outlet (PVO) located at the distal end of the device, eliminating the need for individual vents at each chamber. By reducing direct exposure to ambient air and using non-permeable laminate materials, the platform suppresses evaporation while maintaining reliable bubble-free operation—critical for low-abundance biomarkers such as cortisol.

3.2 Capillary valve

Precise, self-regulated control of fluid progression without external actuation remains a central challenge in passive microfluidics. In Cap-Sweat, this control is achieved using capillary valves—microstructures that regulate flow by introducing controlled variations in channel geometry and surface wettability, thereby modulating local capillary pressure. By generating localized pressure barriers or thresholds, these valves govern fluid advancement within the network. Capillary valves are typically classified as SVs, burst valves, trigger valves, or retention barriers.

Each type leverages tailored interfacial energy landscapes to guide or restrain flow at specific locations within the device. While extensively applied in soft lithography-based devices, capillary valve integration within laser-fabricated, multilayer microfluidics remains underdeveloped.[40] In this work, we demonstrate the direct incorporation of capillary valve functionalities into Cap-Sweat using CO_2 laser-patterned PSA films and PET substrates, enabling precise flow control without secondary surface modification or deposition steps (Fig. 3).[41]

To systematically characterize capillary valve function, a modular testbed was designed comprising two adjacent CHs —designated CH1 and CH2—interconnected by a narrow bridge channel that serves as the air conduit. This simplified architecture recapitulates the sequential CH arrangement and integrated ventilation structure of the Cap-Sweat system (Fig. 3a). The fluidic interfaces of interest are defined as boundary B1, positioned between CH1 and the bridge

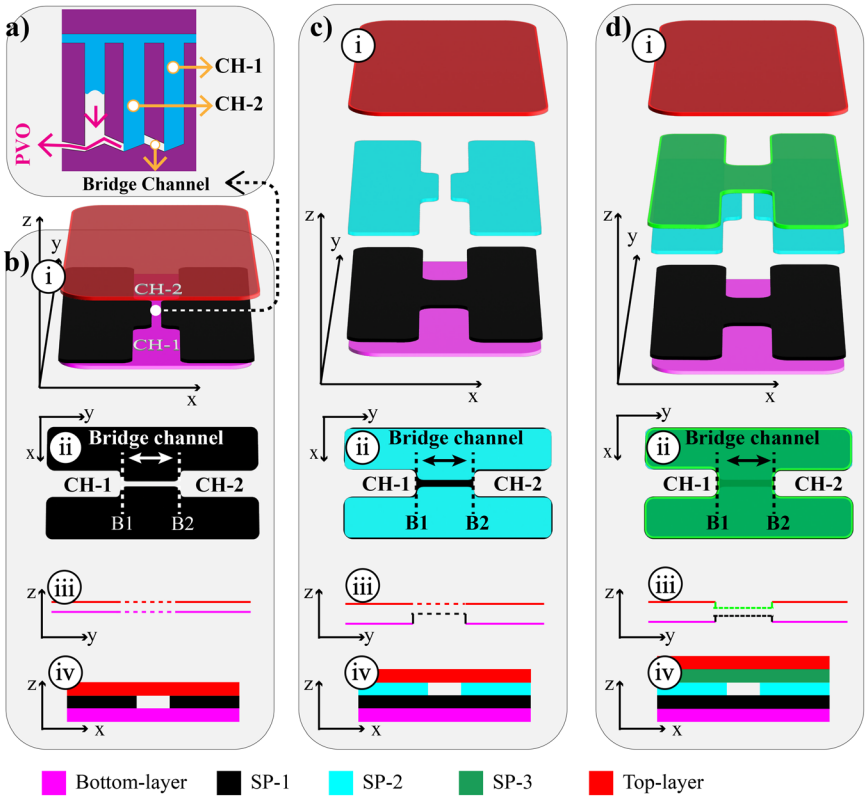

Fig. 3 Valve configurations implemented *via* multilayer laser-cut microfabrication for passive flow control. (a) Schematic representation of a generic test architecture, consisting of two sequential chambers (CH-1 and CH-2) separated by a bridge channel to emulate key boundaries (B1 and B2) within Cap-Sweat. (b) Config-1: (i) exploded view of three-layer stack showing a hydrophobic spacer (black) enclosed by hydrophilic PET layers (purple and red); (ii) top-down layout of CH-1, CH-2, and the intermediate bridge channel; (iii) cross-sectional side view illustrating constant channel height (100 μm); (iv) front-facing view highlighting symmetrical wettability and geometry across boundaries B1 and B2. (c) Config-2: (i) exploded view including an additional hydrophobic SP layer (cyan) to increase capillary resistance; (ii) top view depicting increased wettability contrast; (iii) side view showing stacked hydrophobic layers; (iv) front view demonstrating mixed wettability at B1 and burst valve behavior at B2. (d) Config-3: (i) exploded structure using two hydrophobic SPs (green) to fully encapsulate the bridge channel; (ii) top view; (iii) side view showing increased CH height (300 μm) and reduced bridge height (100 μm); (iv) front view illustrating complete hydrophobic confinement at B1 to achieve effective stop valve (SV) operation.

channel, and boundary B2, located between the bridge and CH2.

Here we introduced three different testbed configurations, referred to as Config-1 through Config-3, each evaluated in two variants: F and G, as discussed earlier in the context of Cap-Sweat (Fig. 2a), all compatible with layer-by-layer laser fabrication. In the F variant, both the top and bottom layers are made of hydrophilic materials, maximizing capillary force for efficient flow. In contrast, the G variant replaces one of these layers with a hydrophobic material, which reduces capillary force in the main and bridge channels but allows for easier drop-casting of functional materials.

The F variant of Config-1, illustrated in Fig. 3b, utilizes geometric constriction as the primary mechanism for modulating capillary flow. In this configuration, CH1 and CH2 are fabricated with uniform channel heights of 100 μm and are interconnected *via* a narrower bridge channel of equal height but reduced width. The device architecture consists of a three-layer laminate: a central hydrophobic PSA (ARcare 8939) flanked by two hydrophilic PET films (3M 9984), as shown in Fig. 3b(i). At boundary B1—the interface between CH1 and the bridge channel—the fluid encounters a geometric constriction that increases hydraulic resistance and modifies the local capillary pressure, consistent with predictions from the Young–Laplace equation (Note S1.2). However, this impedance remains below the threshold required to halt flow, allowing capillary action to proceed uninterrupted through B1 into the bridge (Fig. 3b(ii)). The minimum achievable bridge width is constrained to 200 μm by CO_2 laser fabrication limits. A side profile of Config-1 (Fig. 3b(iii)) demonstrates consistent vertical dimensions across CHs and the bridge, while the frontal cross-section (Fig. 3b(iv)) highlights the layered construction and internal geometry governing flow behavior.

The F variant of Config-2 (Fig. 3c) combines both geometric constriction and material heterogeneity to enhance capillary flow control. In this design, two stacked layers of hydrophobic PSA (ARcare 8939) are employed as SPs, enclosed between hydrophilic PET sealing films (3M 9984), as depicted in Fig. 3c(i). This configuration increases the

number of hydrophobic surfaces at boundary B1 to three, significantly lowering local wettability and elevating the capillary entry pressure. While one hydrophilic surface remains, the dominant hydrophobic environment suppresses fluid advance and effectively slows down progression through the bridge channel. At boundary B2, the combination of reduced channel width and elevated hydrophobicity creates a burst valve behavior—fluid halts until sufficient internal pressure overcomes the retention force, after which it proceeds into CH2 (Fig. 3c(iii)). Although burst valves are not critical to Cap-Sweat's chrono-sampling functionality, this configuration demonstrates their potential utility in timing-dependent assays or fluidic gating schemes. The cross-sectional view in Fig. 3c(iv) delineates the multilayer architecture and spatial arrangement of wettability contrasts, highlighting the distinct fluidic boundaries and valve control regions.

The Config-3 F variant (Fig. 3d) implements a high-resistance architecture by embedding the bridge channel between two hydrophobic SPs, while preserving hydrophilic channel walls in CH1 and CH2. As illustrated in Fig. 3d(i), this configuration effectively nullifies the forward capillary force at boundary B1, converting it into a fully functional SV. The wettability contrast eliminates fluid ingress into the bridge channel, enabling precise flow arrest. This mode is particularly suited for scenarios in which the bridge serves as a ventilation pathway rather than a fluid conduit. For application-relevant performance, CH1 and CH2 heights are increased to 300 μm to accommodate larger sweat volumes, while the bridge channel height remains at 100 μm, achieved by layering three PSA sheets with distinct cut geometries (Fig. 3d(iii)). At boundary B2, the convergence of geometric narrowing and elevated surface energy barrier gives rise to a trigger valve, wherein flow is reinstated only after overcoming a defined threshold pressure. The front-view schematic in Fig. 3d(iv) confirms full hydrophobic encapsulation at B1 and highlights the stratified assembly across SPs, demonstrating controlled modulation of capillary pressure through combined material and structural engineering.

The G variant of each configuration is formed by replacing the hydrophilic top layer (red in Fig. 3) with a hydrophobic one. In Config-1, this change increases the number of hydrophobic surfaces at boundary B1 from two to three, but B1 still fails to function as a reliable SV. In contrast, the G variant of Config-2 (Fig. 3c(iv)) increases B1′ s hydrophobic surfaces from three to four, creating a robust capillary barrier that effectively halts fluid advance. The findings demonstrate that surface wettability, rather than geometric modification, is the dominant factor governing valve functionality. Config-3 is not compatible with the Type-G architecture because Type-G incorporates only two SP layers in the middle layer, whereas Config-3 requires three. Cross-sectional views of the functional capillary elements in the Cap-Sweat Type-G and Type-F architectures are shown in detail in Fig. S1. Config-2 is implemented in the Type-G design, whereas Config-3 is incorporated into Type-F. Although both configurations are fully functional, the Type-F architecture was used in this study because it accommodates a larger sweat volume per CH, as required for ELISA analysis.

3.3 Ventilation capillary circuits

In conventional microfluidic devices for sweat collection, each CH is typically equipped with an individual air vent to facilitate displacement of trapped air during sample ingress, thereby supporting smooth, bubble-free filling.[6,29,42–44] These vents are commonly located at the far end of each CH (Fig. 4a(i)) to enable local air release as sweat enters the fluidic compartment. While this approach is effective in ensuring hydraulic continuity, it introduces critical limitations when applied to wearable chrono-sampling systems.[45] Specifically, each open vent becomes a direct site for evaporative loss, particularly under high-transpiration conditions such as physical exertion, where increased ambient temperature and skin airflow accelerate moisture evaporation. This loss is most pronounced in the first CH, which remains vented throughout the entire sampling period and is thus continuously exposed to evaporative flux. Such evaporation not only reduces the collected volume but also disrupts the temporal integrity of the sample. As water escapes through the vent, it is replaced by newly secreted sweat, leading to undesired mixing between early and late secretions within the same compartment. This backfilling effect compromises the chronological resolution of the sample array, which is essential for accurate temporal tracking of dynamic biomarker fluctuations. Moreover, evaporation-induced concentration effects may alter the apparent analyte levels, introducing systematic bias into quantitative assays. Consequently, minimizing evaporative loss is paramount in chrono-sampling applications, where time-resolved biomolecular fidelity directly underpins diagnostic relevance and physiological interpretation.

To circumvent the limitations associated with individual venting, the Cap-Sweat system incorporates a centralized capillary ventilation network. Two distinct architectures were designed and evaluated: a parallel CC configuration and a series CC configuration. In the parallel CC (Fig. 4a(ii)), each collection CH is connected to a single PVO through dedicated microchannels that function as passive air conduits. This design replaces multiple exposed vents with a singular exit point, substantially reducing the total venting surface area exposed to the environment and thereby mitigating evaporative losses. The extended conduit length between each CH and the PVO introduces an additional barrier to vapor diffusion, acting as a spatial buffer against ambient air intrusion. Importantly, this architecture ensures independent venting for each CH, such that the air displacement required for filling one CH does not interfere with or depend on the filling state of adjacent CHs.

In contrast, the series CC configuration (Fig. 4a(iii), Fig. 2c(ii)) arranges the air conduits such that venting is

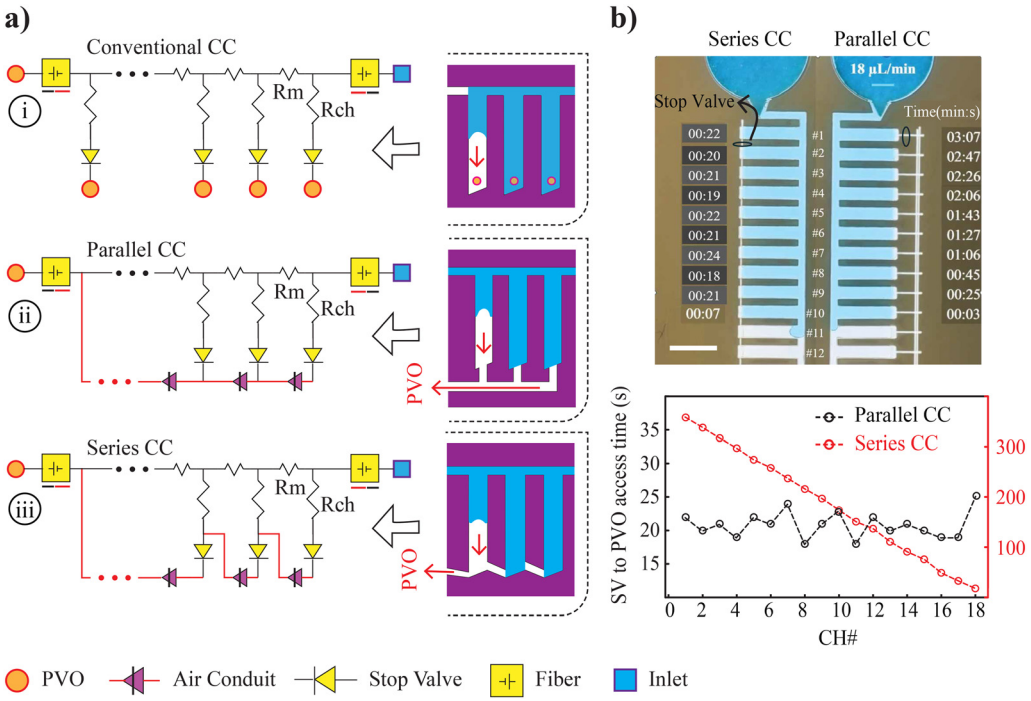

Fig. 4 Comparative analysis of capillary ventilation strategies in wearable chrono-sampling. (a) Schematic representations of ventilation network architectures. Hydraulic resistances of the main connector channel and CHs are denoted as Rm and Rch: (i) conventional CH-specific venting with individual access to ambient air, (ii) parallel CC system linking each CH independently to a shared PVO, and (iii) series CC configuration where CHs are sequentially vented through a cascading air path. Right panels show corresponding fluidic layouts. (b) *In vitro* comparison of stop-valve access to the PVO at the downstream end of each CH in the parallel and series CC configurations, with liquid introduced using a syringe pump at a flow rate of 18 μL min^{-1}.

achieved sequentially, with each CH's outlet connected in a cascading manner along a common path to the PVO. In this architecture, the progression of filling inherently alters the ventilation landscape: as a downstream CH becomes occupied, it blocks the venting access of its upstream neighbor. Consequently, each CH experiences only a transient ventilation window. In the presence of an SV at the downstream end of each CH, this window begins when the advancing liquid front reaches the SV of CH x and terminates when the liquid front reaches the SV of the subsequent CH (x + 1). While the series configuration maintains effective chrono-integrity by supporting discrete CH filling, it imposes tighter constraints on the timing of fluid ingress. However, the predesigned hydraulic resistance of the CHs and MF (Note S1.3), together with the series CC ventilation network, enables bubble-free filling and reliable chrono-sampling, despite the stricter temporal constraints compared with the parallel CC configuration.

Both ventilation architectures eliminate the need for multiple chamber-specific (CH-specific) vents, thereby reducing direct exposure to ambient air and limiting vapor diffusion pathways. Compared with conventional designs, this centralized ventilation approach improves sample preservation, particularly for low-abundance analytes and extended-duration sampling. In the following section, we evaluate and select the appropriate CC configuration based on the properties of the sample solution and the reliability of stop-valve operation.

3.4 Capillary circuit selection informed by surface wettability and functional reliability

Reliable chrono-sampling in Cap-Sweat depends on robust fluid control through passive CC. Among the valve configurations evaluated, the F variant of Config-3 and the G variant of Config-2 each incorporate a four-surface hydrophobic SV, enabling compatibility with both parallel and series CC designs. While these valves operate effectively with deionized water, they exhibit diminished performance under physiological conditions due to the lower surface tension of human sweat. Specifically, the SP materials used in these designs exhibit modest hydrophobicity, with contact angles of approximately 90° for water and ~83° for artificial sweat. Under these conditions, minor variations in surface energy or channel geometry can weaken the effective capillary barrier, permitting slow fluid leakage across the SV into adjacent CHs and thereby compromising isolation.

To mitigate this limitation, the CC architecture needs to minimize the duration for which the SV maintains access to the PVO after first contact with the advancing liquid. Accordingly, once the liquid reaches the SV at the downstream end of each CH, the available time for liquid penetration through the valve is insufficient—even for

sidewall contact angles in the range of 83–90°. *In vitro* tests (Fig. 4b and Movie S1) were performed using Cap-Sweat devices comprising 18 sequential CHs, with liquid introduced *via* a syringe pump at a flow rate of 18 μL min^{-1}. The SV-to-PVO access time was quantified for both series and parallel CC configurations.

The series configuration exhibited substantially shorter collection chamber (CH) access times to the primary vent outlet (PVO), thereby limiting the duration of stop-valve exposure and reducing the probability of leakage. In contrast, the parallel configuration maintains prolonged connectivity to the PVO, increasing the likelihood of unintended stop-valve opening. This difference arises because, in the series CC design, each CH's connection to the PVO is terminated once the downstream chamber fills, effectively sealing the air conduit and reducing the risk of evaporation and backflow. On the other hand, parallel CCs maintain continuous PVO connectivity across all CHs, such that early-filled compartments, particularly the first CH, remain vented throughout the sampling sequence. This persistent access amplifies the chance of valve breach, especially under low contact angle conditions, thereby increasing the risk of temporal cross-contamination.

Accordingly, the series CC architecture is favored for implementation in Cap-Sweat. This design capitalizes on the inherent dynamics of sequential CH filling: the next CH is filled and closed before leakage can occur through the preceding SV. Although the SVs do not function as absolute barriers under moderate hydrophobicity, the time-dependent isolation intrinsic to the series CC provides sufficient containment. This dynamic gating mechanism enables reliable chrono-separation without additional actuation, material modification, or post-fabrication sealing steps, thereby preserving platform simplicity and manufacturability.

3.5 Incorporation of fiber wicking element at the inlet

To facilitate rapid fluid transfer from the epidermal surface to the microchannel network, Cap-Sweat integrates a fiber-based wicking pad within its inlet architecture (Fig. 2). This embedded fiber acts as a capillary conduit, bridging the skin-device interface and minimizing dead volume—the initial void space between the skin and the microfluidic entrance that must be filled before fluid propagation begins. By establishing a continuous capillary pathway, the fiber enables direct sweat uptake and accelerates fluid transport to the channel entrance.

Although the fiber does not contribute to fluid storage within the collection CHs, it plays a critical role in system priming and flow initiation. To further reduce saturation time and enhance flow directionality, micro perforations were manually introduced into the fiber structure. These perforations facilitate localized saturation and channel-directed flow, thereby improving volumetric throughput and temporal response.

The effect of the fiber was evaluated using an *in vitro* assay described in detail in the SI and shown in Fig. S2. Based on this analysis, Table S1 summarizes the influence of fiber integration on dead-volume reduction across all Cap-Drop variants, with the Type G design achieving an 83% reduction under *in vitro* conditions. This improvement arises not only from volumetric displacement by the wicking fiber, but also from the presence of a sharp fiber tip, which effectively eliminates the burst valve located at the inlet–microchannel interface (Fig. S2b.II). Previous studies have demonstrated that the addition of hydrophilic filler materials at this interface can eliminate the saturation delay altogether and increase transfer efficiency;[20] however, such strategies typically require multi-step surface treatment or material modification, which adds complexity to fabrication.

As shown in Fig. S2b.I, liquid does not enter hydrophobic base devices regardless of injected volume or fiber incorporation, indicating that such platforms rely on complete inlet filling and elevated glandular pressure to overcome the entry barrier. In narrow hydrophobic channels, capillary resistance further exceeds physiologically generated glandular pressure, preventing spontaneous flow initiation. In contrast, hydrophilic Cap-Sweat configurations utilize capillary forces as the primary driving mechanism, allowing the fiber to wick sweat efficiently from the skin and propagate it through the microfluidic network. Beyond facilitating fluid delivery, the fiber also minimizes air intrusion, maintaining a stable, bubble-free interface during dynamic operation.

3.6 *In vitro* validation of chrono-sampling fidelity

Sweat chrono-sampling enables dynamic monitoring of biomarker fluctuations—such as cortisol, lactate, and electrolytes—offering a non-invasive window into acute physiological processes.[5,29] Prior to *in vivo* deployment, Cap-Sweat's temporal fidelity was evaluated using a programmable *in vitro* platform with dual-color dye tracers as optical analogs of time-varying biomarker concentrations. Two chromogenic solutions—one yellow and one purple—were delivered to the device inlet *via* independently actuated syringe pumps. Each pump was programmed with time-dependent flow rate profiles (Fig. S3), generating a controlled dynamic input that mimicked physiological biomarker fluctuations during exercise or stress response. The evolving input color served as a visually trackable surrogate for biomolecular concentration changes over time. As fluid entered the Cap-Sweat microfluidic architecture, the sequentially arranged collection CHs acted as spatiotemporal digitizers, capturing discrete aliquots of the dynamic input. This setup enabled direct assessment of temporal resolution and cross-contamination resistance under well-defined, time-varying conditions.

Following sample collection, each CH was optically imaged under controlled lighting conditions, and its contents were subjected to hue–saturation–value (HSV) analysis. The

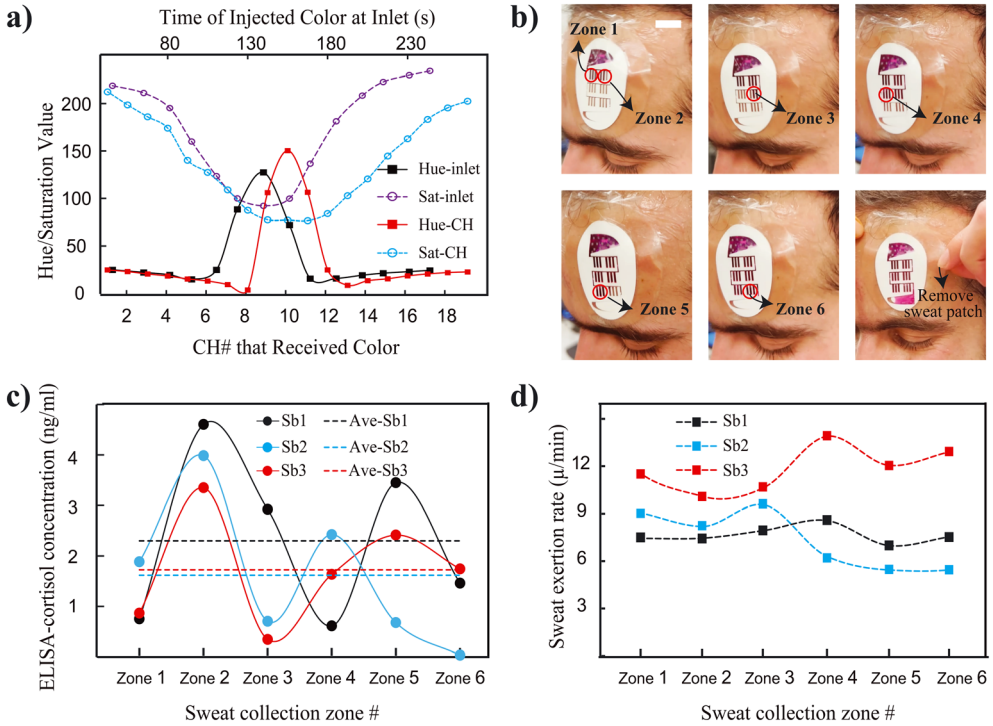

Fig. 5 Design and functionality of Cap-Sweat for chrono-sampling of sweat biomarkers and secretion dynamics. (a) *In vitro* validation of temporal fidelity, where alternating purple and yellow dyes were injected through the inlet, producing a color gradient across CHs and demonstrating continuous tracking capability of biomarker fluctuations. (b) On-body application of Cap-Sweat in human volunteers showing six sequential sampling zones. Scale bar: 2 cm. (c) Time-resolved cortisol concentration profiles from three subjects, determined *via* ELISA from sweat collected across six zones. (d) Corresponding sweat excretion rates measured across six zones from three subjects, enabling high-resolution quantification of dynamic sweat secretion kinetics. Together, these data highlight Cap-Sweat's dual capability for non-invasive, time-resolved assessment of both biomarker secretion and sweat physiology.

extracted chromatic data were temporally mapped and compared to the theoretical inlet profile. As shown in Fig. 5a, the recorded colorimetric patterns exhibited high concordance with the programmed input sequence, demonstrating that the device accurately encoded dynamic inputs into spatially resolved sample compartments. Minor temporal shifts were observed in the initial CHs, attributable to the fluidic delay introduced by the MF channel volume, which acts as a temporal buffer between the inlet and the first CH. Importantly, no evidence of dye dispersion or inter-CH mixing was detected beyond this initial lag phase, confirming the effectiveness of the capillary barrier valves in isolating consecutive fluid volumes. The precision of temporal sampling improved progressively across downstream CHs, indicating steady-state operation and minimal influence from pulsatile flow irregularities.

The results validate the chrono-sampling capability of Cap-Sweat under physiologically relevant flow conditions, demonstrating accurate discretization of dynamic input concentrations without external actuation. Further optimization—such as reduction of channel dead volume or refinement of inlet resistance—could yield even greater temporal accuracy, reinforcing the potential of this platform for continuous monitoring of labile or pulsatile biomarkers in wearable applications.

3.7 Cortisol chrono-sampling and physiological interpretation

Following successful *in vitro* characterization, Cap-Sweat was deployed *in vivo* to assess its performance under physiologically relevant conditions involving moderate-intensity physical exertion (Movie S2). For all *in vivo* experiments, Cap-Sweat Type-F incorporating a series CC architecture with Config-3 SVs was used, as this configuration provides the larger per-CH sweat volume required for ELISA-based cortisol analysis. Human subjects (n = 3) performed treadmill exercise at a controlled pace of 5.5–6.5 km h^{-1} (1.5% incline), a regimen previously shown to induce thermoregulatory eccrine sweating without causing excessive motion artifacts or sweat pooling.[46,47] This specific protocol was chosen to ensure consistent sweat generation across subjects while minimizing factors that could disrupt capillary filling, such as vigorous limb movement or excessive gland pressure. Exercise sessions lasted 12–16 min, corresponding to sustained eccrine activation under moderate workload (Fig. 5b) and matching the full 18-CH chrono-sampling window (40–60 s per CH). This ensured that each chamber captured newly secreted sweat while avoiding thermal fatigue and preserving steady-state physiological output for cortisol evaluation.

To ensure sufficient volume for downstream analysis, samples from every three CHs—corresponding to ~2–3 min of sweat collection—were pooled to yield a 9 μL aliquot for ELISA-based cortisol quantification. Fig. 5c displays representative cortisol trajectories from three participants, each revealing unique temporal dynamics. All participants showed a pronounced early peak within the first 2–3 min of physical exertion, followed by a drop and subsequent fluctuations. This early cortisol surge likely reflects rapid transdermal diffusion driven by steep plasma-to-sweat concentration gradients or the release of preformed cortisol from sweat glands under acute sympathetic stimulation.[11] The fluctuating patterns that follow suggest pulsatile secretion dynamics of the hypothalamic–pituitary–adrenal (HPA) axis and/or reabsorptive processes within the sweat duct.[48,49] While such dynamic trends are typically missed in low-resolution sampling methods, the sub-minute chrono-sampling enabled by Cap-Sweat reveals fine-grained hormonal variations relevant to acute stress physiology. Notably, when the cortisol profiles were transformed into the frequency domain, low-frequency oscillatory components (~0.05–0.15 Hz) emerged, consistent with known ultradian rhythms of cortisol regulation described in plasma studies. This suggests that Cap-Sweat can resolve meaningful physiological patterns associated with stress adaptation and neuroendocrine pulsatility—offering a wearable platform for continuous endocrine monitoring beyond conventional static assays.

3.8 Sweat secretion kinetics and dual-mode functionality

Fig. 5d presents sweat-rate data across six zones during the exercise period for three human subjects (Sb), where each zone comprises three consecutive CHs connected in series (total volume: 9 μL). Analyzing sweat volume at the level of individual CHs, rather than as zone-aggregated measurements, provides improved temporal resolution (Fig. S4 and S5), with observed trends consistent with physiological patterns reported in the literature (Note S4). Because each CH stores a fixed volume, variations in sweat secretion rate affect only the filling time and not the measured biomarker concentration. Accordingly, differences in cortisol levels across zones (Fig. 5c), quantified by ELISA, reflect genuine temporal concentration dynamics rather than artifacts arising from sweat-rate variability. This decoupling of secretion rate from analyte concentration enables Cap-Sweat to operate as a dual-mode lab-on-chip platform for simultaneous assessment of thermoregulation and stress response. The system achieves <3 min temporal resolution per CH through passive capillary transport, eliminating the need for active pumping. This architecture further supports integration of sweat-rate modeling with chrono-sampled biomarker data, providing a foundation for estimating secretion kinetics, gland responsiveness, and dynamic stress load indices in future wearable applications.

3.9 Platform extensibility and physiological integration

Beyond acute exercise studies, Cap-Sweat's platform architecture is extensible to multi-hour and multiplexed biomarker tracking. Its passive capillary elements and modular CHs support delayed filling strategies, enabling longitudinal studies without continuous exertion. This opens new avenues for use in sedentary or sleep-monitoring contexts, psychological health surveillance, and occupational fatigue assessment. Furthermore, integration of naked-eye sensors (*e.g.*, colorimetric strips) or embedded electrochemical transducers within individual sampling units can provide instant readouts of pH, glucose, or lactate fluctuations—mirroring concepts established in wearable diagnostic platforms.[50] Such visual or digital readouts could inform users of hourly metabolic changes, thereby enhancing self-monitoring and preventative care.

While cortisol is widely used for non-invasive stress assessment, its response kinetics (10–30 min) primarily reflect downstream activation of the hypothalamic–pituitary–adrenal (HPA) axis and may therefore miss rapid-onset stressors occurring on seconds-to-minutes timescales. The high temporal resolution of Cap-Sweat provides a foundation for detecting acute-phase sweat biomarkers (*e.g.*, neuropeptides, catecholamines, and cytokines) and for integrating immunosensors that enable simultaneous monitoring of both acute and chronic stress responses. Such capability could improve attribution of physiological triggers and differentiation of stress response types. Acute mediators, including calcitonin gene-related peptide (CGRP), substance P, and interleukin-6 (IL-6), have been associated with eccrine secretion and peripheral neurogenic inflammation[51,52] and may accumulate in superficial tissue layers accessible to wearable sweat sensors. Incorporating corresponding sensing elements into Cap-Sweat microchannels or detection zones could enable continuous electrochemical or optical monitoring of dermal neurochemical activity.

Cap-Sweat's compact design, which does not require external adhesives, enables placement on multiple body sites (*e.g.*, forehead, forearm, chest, upper back) without disrupting natural sweat flow. This supports simultaneous multi-patch deployment for spatial mapping of biomarker dynamics across anatomical regions. Given regional differences in sweat gland density and subtype distribution, multi-site chrono-sampling can reveal site-specific variations in sweat composition, secretion rate, and biomarker flux. Capturing this spatial heterogeneity may enhance diagnostic interpretation and facilitate identification of biomarkers enriched within localized skin microenvironments. By enabling site-resolved biomarker profiling, multi-patch deployment positions Cap-Sweat as a versatile platform for advancing personalized diagnostics and improving our understanding of regional dermal physiology.

A key next step is integrating physiological models of skin transport with on-chip CC design. Current analyses

often treat sweat secretion as discrete input pulses without explicitly accounting for upstream fluid generation, interstitial transport, or epidermal reabsorption. In practice, eccrine secretion reflects coupled vasodilation, aquaporin-mediated transport, ductal ionic exchange, and feedback regulation that shape both flow rate and molecular composition at the skin surface. Incorporating computational models that simulate glandular secretion, interstitial transport, and epidermal diffusion kinetics, in conjunction with the physical design of the capillary microfluidic architecture, will enable the derivation of mechanistic correlations between observed secretion patterns and upstream physiological events. This framework could also enable frequency-domain analysis of sweat biomarkers to identify periodicities associated with autonomic rhythms or hormonal pulsatility. Overall, coupling tissue-level transport modeling with CC design may improve mechanistic interpretation of time-resolved sweat signals relevant to stress and metabolism.

Conclusion

This study presents Cap-Sweat, a capillary-driven, laser-fabricated lab-on-chip platform for passive, temporally resolved sweat sampling under physiological conditions. By relying on capillary transport without external pumping or applied pressure, the system preserves natural sweat secretion while minimizing flow perturbation. An optimized venting architecture suppresses evaporation and back-contamination, while capillary control structures and embedded SVs regulate fluid progression into 18 discrete, fixed-volume CHs. This design enables sub-minute chrono-sampling and supports concurrent analysis of sweat secretion kinetics and biomarker dynamics. In human subjects, Cap-Sweat captured characteristic sweat-rate profiles, including an early transient peak within the first 3–5 min of exertion, followed by a lower, fluctuating secretion regime. In parallel, time-resolved cortisol measurements revealed dynamic, subject-dependent patterns consistent with acute sympathetic activation. The findings demonstrate that high-resolution chrono-sampling can resolve endocrine and thermoregulatory dynamics that are obscured by conventional bulk sweat collection methods. Cap-Sweat's compact, skin-conformal design supports placement across multiple anatomical sites, enabling investigation of regional secretion patterns and site-specific biomarker flux. The platform's modular architecture and sensor compatibility may facilitate multiplexed detection beyond cortisol and extended-duration sampling under sedentary or low-sweat conditions. Future integration of computational models of glandular secretion, dermal transport, and microfluidic dynamics with chrono-sampled data may further enhance mechanistic interpretation and predictive analysis of sweat biomarker kinetics in response to physiological stressors.

Author contributions

P. J. and A. S. N. contributed to conceptualization and methodology. P. J. performed investigation, device fabrication, data curation, and formal analysis, and prepared the visualization and writing – original draft. P. J. and A. S. N. contributed to writing – review & editing and interpretation of the results. All authors reviewed and approved the final manuscript.

Conflicts of interest

The authors declare no conflicts of interest.

Data availability

The data that support the findings of this study are available from the corresponding author upon reasonable request.

Supplementary information (SI) is available. See DOI: https://doi.org/10.1039/d5lc01172h.

Acknowledgements

The authors acknowledge the Natural Sciences and Engineering Research of Canada (NSERC); Canada Research Chair; Canadian Institutes of Health Research (CIHR); Alberta Innovates, We-Trac NSERC CREATE program, and CMC – Microsystems, Canada for supporting this research.

References

1 K. M. Clark and T. R. Ray, *ACS Sens.*, 2023, **8**, 3606–3622.
2 S. Jo, D. Sung, S. Kim and J. Koo, *Biomed. Eng. Lett.*, 2021, **11**, 117–129.
3 E. K. Adam, M. E. Quinn, R. Tavernier, M. T. McQuillan, K. A. Dahlke and K. E. Gilbert, *Psychoneuroendocrinology*, 2017, **83**, 25–41.
4 S. Mercadante and A. Bellastella, *Life*, 2024, **14**, 546.
5 A. Vaquer, E. Barón and R. de la Rica, *ACS Sens.*, 2022, **7**, 488–494.
6 J. Choi, D. Kang, S. Han, S. B. Kim and J. A. Rogers, *Adv. Healthcare Mater.*, 2017, **6**(5), 1601355.
7 Z. Zhang, Z. Li, K. Wei, Z. Cao, Z. Zhu and R. Chen, *Talanta*, 2024, 125865.
8 N. Brasier, C. Niederberger, M. Zanella, A. Othman, R. Schlapbach, L. Kunz, A. Dittmann, K. Reeve, M. Prummer and J. Goldhahn, *Commun. Biol.*, 2025, **8**, 650.
9 S.-R. Kim, Y. Zhan, N. Davis, S. Bellamkonda, L. Gillan, E. Hakola, J. Hiltunen and A. Javey, *Nat. Electron.*, 2025, 1–9.
10 P. Pirovano, M. Dorrian, A. Shinde, A. Donohoe, A. J. Brady, N. M. Moyna, G. Wallace, D. Diamond and M. McCaul, *Talanta*, 2020, **219**, 121145.
11 R. M. Torrente-Rodríguez, J. Tu, Y. Yang, J. Min, M. Wang, Y. Song, Y. Yu, C. Xu, C. Ye and W. W. IsHak, *Matter*, 2020, **2**, 921–937.
12 F. Gao, C. Liu, L. Zhang, T. Liu, Z. Wang, Z. Song, H. Cai, Z. Fang, J. Chen and J. Wang, *Microsyst. Nanoeng.*, 2023, **9**, 1.

13 L. B. Baker, J. B. Model, K. A. Barnes, M. L. Anderson, S. P. Lee, K. A. Lee, S. D. Brown, A. J. Reimel, T. J. Roberts and R. P. Nuccio, *Science*, 2020, **6**, eabe3929.
14 H. Y. Y. Nyein, M. Bariya, L. Kivimäki, S. Uusitalo, T. S. Liaw, E. Jansson, C. H. Ahn, J. A. Hangasky, J. Zhao and Y. Lin, *Science*, 2019, **5**, eaaw9906.
15 Y. Sun, J. Wang, Q. Lu, T. Fang, S. Wang, C. Yang, Y. Lin, Q. Wang, Y.-q. Lu and D. Kong, *ACS Nano*, 2024, **18**, 2335–2345.
16 N. Twine, R. Norton, M. Brothers, A. Hauke, E. Gomez and J. Heikenfeld, *Lab Chip*, 2018, **18**, 2816–2825.
17 A. Hauke, P. Simmers, Y. Ojha, B. Cameron, R. Ballweg, T. Zhang, N. Twine, M. Brothers, E. Gomez and J. Heikenfeld, *Lab Chip*, 2018, **18**, 3750–3759.
18 J. C. Spinelli, B. J. Suleski, D. E. Wright, J. L. Grow, G. R. Fagans, M. J. Buckley, D. S. Yang, K. Yang, S. M. Beil and J. C. Wallace, *npj Digit. Med.*, 2025, **8**, 76.
19 M. Bariya, N. Davis, L. Gillan, E. Jansson, A. Kokkonen, C. McCaffrey, J. Hiltunen and A. Javey, *ACS Sens.*, 2022, **7**, 1156–1164.
20 H. Y. Y. Nyein, M. Bariya, B. Tran, C. H. Ahn, B. J. Brown, W. Ji, N. Davis and A. Javey, *Nature*, 2021, **12**, 1823.
21 J. Tu, J. Min, Y. Song, C. Xu, J. Li, J. Moore, J. Hanson, E. Hu, T. Parimon and T.-Y. Wang, *Nature*, 2023, **7**, 1293–1306.
22 S. Apoorva, N.-T. Nguyen and K. R. Sreejith, *Lab Chip*, 2024, **24**, 1833–1866.
23 C. Liu, T. Xu, D. Wang and X. Zhang, *Talanta*, 2020, **212**, 120801.
24 S. Coyle, K.-T. Lau, N. Moyna, D. O'Gorman, D. Diamond, F. Di Francesco, D. Costanzo, P. Salvo, M. G. Trivella and D. E. De Rossi, *IEEE Trans. Inf. Technol. Biomed.*, 2010, **14**, 364–370.
25 F. Zhao, M. Bonmarin, Z. Chen, M. Larson, D. Fay, D. Runnoe and J. Heikenfeld, *Lab Chip*, 2020, **20**, 168–174.
26 M. C. Brothers, M. DeBrosse, C. C. Grigsby, R. R. Naik, S. M. Hussain, J. Heikenfeld and S. S. Kim, *Acc. Chem. Res.*, 2019, **52**, 297–306.
27 T. Kaya, G. Liu, J. Ho, K. Yelamarthi, K. Miller, J. Edwards and A. Stannard, *Electroanalysis*, 2019, **31**, 411–421.
28 C. Wang, Z. Wang, W. Wei, Z. Zhang, A. A. Li, G. Huang, X. Li, S. S. Ge, L. Zhou and H. Kong, *npj Flexible Electron.*, 2024, **8**, 47.
29 S. Shajari, R. Salahandish, A. Zare, M. Hassani, S. Moossavi, E. Munro, R. Rashid, D. Rosenegger, J. S. Bains and A. Sanati Nezhad, *Adv. Sci.*, 2023, **10**, 2204171.
30 Y. Zhang, H. Guo, S. B. Kim, Y. Wu, D. Ostojich, S. H. Park, X. Wang, Z. Weng, R. Li and A. J. Bandodkar, *Lab Chip*, 2019, **19**, 1545–1555.
31 S. H. Cho, S. Cho, Z. Lv, Y. Sekine, S. Liu, M. Zhou, R. F. Nuxoll, E. E. Kanatzidis, R. Ghaffari and D. Kim, *Lab Chip*, 2025, **25**, 1647–1655.
32 W. Liu, H. Cheng and X. Wang, *npj Flexible Electron.*, 2023, **7**, 43.
33 D. Mark, S. Haeberle, G. Roth, F. Von Stetten and R. Zengerle, *Microfluidics based microsystems: fundamentals and applications*, 2010, pp. 305–376.
34 H.-s. Kim, S. Michielsen and E. DenHartog, *Colloids Surf., A*, 2021, **622**, 126726.
35 Y. Sun, J. Wang, Q. Lu, J. Zhang, Y. Li, Y. Pang, C. Yang, Q. Wang and D. Kong, *ACS Sens.*, 2024, **9**, 1515–1524.
36 J. R. Sempionatto, A. A. Khorshed, A. Ahmed, A. N. De Loyolae Silva, A. Barfidokht, L. Yin, K. Y. Goud, M. A. Mohamed, E. Bailey and J. May, *ACS Sens.*, 2020, **5**, 1804–1813.
37 Y. Wu, E. E. Kanatzidis, R. Avila, M. Zhou, Y. Bai, S. Chen, Y. Sekine, J. Kim, Y. Deng and H. Guo, *Mater. Horiz.*, 2023, **10**, 4992–5003.
38 D. S. Yang, M. Zhou, S. Li, S. Cho, Y. Wu, Y. Sekine, E. E. Kanatzidis, Z. Lv, K. Yamagishi and J. Kim, *Adv. Funct. Mater.*, 2025, e09169.
39 P. Jalali, B. Zarin, A. Zare, S. Abdollahi, M. Hassani, M. Vatani, M. Farrokhnia, R. Salahandish, H. Hejazi and A. Sanati-Nezhad, *Small*, 2025, 2411997.
40 R. Safavieh and D. Juncker, *Lab Chip*, 2013, **13**, 4180–4189.
41 Y. Zhang, Y. Chen, J. Huang, Y. Liu, J. Peng, S. Chen, K. Song, X. Ouyang, H. Cheng and X. Wang, *Lab Chip*, 2020, **20**, 2635–2645.
42 J. Choi, A. J. Bandodkar, J. T. Reeder, T. R. Ray, A. Turnquist, S. B. Kim, N. Nyberg, A. l. Hourlier-Fargette, J. B. Model and A. J. Aranyosi, *ACS Sens.*, 2019, **4**, 379–388.
43 Y. He, L. Wei, W. Xu, H. Wu and A. Liu, *Biosensors*, 2023, **13**, 372.
44 S. Garcia-Rey, E. Gil-Hernandez, U. B. Gunatilake, L. Basabe-Desmonts and F. Benito-Lopez, *Sens. Actuators, B*, 2023, **382**, 133514.
45 A. Olanrewaju, M. Beaugrand, M. Yafia and D. Juncker, *Lab Chip*, 2018, **18**, 2323–2347.
46 A. C. Hackney, *Expert Rev. Endocrinol. Metab.*, 2006, **1**, 783–792.
47 O. Jay, J. D. Périard, L. Hunt, H. Ren, H. Suh, R. R. Gonzalez and M. N. Sawka, *J. Appl. Physiol.*, 2024, **137**, 1014–1020.
48 L. B. Baker and A. S. Wolfe, *Eur. J. Appl. Physiol.*, 2020, **120**, 719–752.
49 S. L. Lightman and B. L. Conway-Campbell, *Nat. Rev. Neurosci.*, 2010, **11**, 710–718.
50 J. Heikenfeld, A. Jajack, J. Rogers, P. Gutruf, L. Tian, T. Pan, R. Li, M. Khine, J. Kim and J. Wang, *Lab Chip*, 2018, **18**, 217–248.
51 L. Marek-Jozefowicz, B. Nedoszytko, M. Grochocka, M. A. Żmijewski, R. Czajkowski, W. J. Cubała and A. T. Slominski, *Int. J. Mol. Sci.*, 2023, **24**, 5001.
52 K. Nordlind, L. Chin, A. Ahmed, J. Brakenhoff, E. Theodorsson and S. Liden, *Arch. Dermatol. Res.*, 1996, **288**, 431–435.